

Wavenumber-Division Multiplexing in Holographic MIMO with NLoS Channels

Ashutosh Prajapati,¹ Prathapasinghe Dharmawansa,¹ Marco Di Renzo,^{2,3} and Italo Atzeni¹

¹ Centre for Wireless Communications, University of Oulu, Finland

² Université Paris-Saclay, CNRS, CentraleSupélec, Laboratoire des Signaux et Systèmes, France

³ King's College London, Centre for Telecommunications Research, Department of Engineering, United Kingdom

Emails: {ashutosh.prajapati, prathapasinghe.kaluwadave, italo.atzeni}@oulu.fi, marco.di_renzo@kcl.ac.uk

Abstract—Wavenumber-division multiplexing (WDM) was introduced as a counterpart of orthogonal frequency-division multiplexing in the spatial-frequency domain for line-of-sight holographic multiple-input multiple-output (MIMO) systems. In this paper, we extend WDM to holographic MIMO channels with non-line-of-sight (NLoS) propagation. We show that applying WDM to the NLoS channel yields the corresponding angular-domain representation, which we characterize through the power spectral factor and power spectral density. We further obtain a closed-form characterization for the case of isotropic scattering, recovering Jakes' isotropic model. The analysis is complemented by numerical results evaluating the degrees of freedom and ergodic capacity under both isotropic and non-isotropic scattering.

Index Terms—Holographic MIMO, near-field communications, wavenumber-division multiplexing.

I. INTRODUCTION

Wireless data demand is growing at an unprecedented pace, pushing communications systems toward higher frequencies where extremely dense deployments of physically small antennas become feasible [1]. This trend has sparked strong interest in holographic multiple-input multiple-output (MIMO) technologies as a means to support future high-capacity networks and intelligent applications. Unlike conventional massive MIMO, where antenna elements are typically spaced about half a wavelength apart to limit spatial correlation [2], holographic MIMO envisions continuous apertures (i.e., surfaces or lines) or densely packed antenna arrays, which become electrically large. In this regime, near-field propagation becomes dominant, in contrast to classical massive MIMO that generally operates under far-field conditions [3]. Holographic MIMO is often realized using programmable metamaterials [4], enabling flexible hardware architectures and multifunctional operation across time, frequency, and space.

The work of A. Prajapati, P. Dharmawansa, and I. Atzeni was supported by the Research Council of Finland (336449 Profi6, 348396 HIGH-6G, and 369116 6G Flagship). The work of M. Di Renzo was supported by the France-Nokia Chair of Excellence in ICT, by the European Union through the Horizon Europe projects COVER (101086228), UNITE (101129618), INSTINCT (101139161), and TWIN6G (101182794), by the Agence Nationale de la Recherche (ANR) through the France 2030 project ANR-PEPR Networks of the Future (NF-Founds 22-PEFT-0010), by the CHIST-ERA project PASSIONATE (CHIST-ERA-22-WAI-04 and ANR-23-CHR4-0003-01), and by the Engineering and Physical Sciences Research Council (EPSRC), part of UK Research and Innovation, and the UK Department of Science, Innovation and Technology through the CHEDDAR Telecom Hub (EP/X040518/1 and EP/Y037421/1) and through the HASC Telecom Hub (EP/X040569/1).

Continuous-aperture MIMO models arise either from the spatial sampling of the transmit and receive apertures, or from expanding the transmit current and received field using suitable basis functions. The latter approach yields the wavenumber-division multiplexing (WDM) framework, introduced in [5] and inspired by orthogonal frequency-division multiplexing (OFDM): while OFDM operates in the frequency domain, WDM enables multiplexing in the wavenumber (spatial-frequency) domain through an orthogonal decomposition of the continuous current and field. Prior WDM studies build on a holographic line model under purely line-of-sight (LoS) propagation [5], [6], whereas non-line-of-sight (NLoS) propagation has been explored only for spatial-sampling-based frameworks [7], [8]. Although millimeter-wave and sub-terahertz systems are often LoS-dominated, small-scale fading remains significant, so NLoS components cannot be entirely neglected.

In this paper, we extend the WDM framework using the NLoS holographic line model introduced in [9] and show that applying WDM to the NLoS channel yields the corresponding angular-domain representation. By analyzing the spatial autocorrelation of the WDM-based NLoS channel, we establish a relation between the power spectral factor (PSF) and power spectral density (PSD), enabling an explicit characterization of the resulting angular-domain channel. We further derive closed-form expressions of the autocorrelation function (ACF) and PSD under isotropic scattering, which allows us to retrieve the classical Jakes' isotropic model. The results demonstrate that WDM serves not only as a multiplexing technique but also as a powerful analytical tool for investigating holographic MIMO channels. Finally, we evaluate the degrees of freedom (DoF) and ergodic capacity of the considered WDM-based NLoS channel and show that both degrade significantly under non-isotropic scattering compared with the isotropic case.

II. SYSTEM MODEL

Consider a WDM-based holographic MIMO system over an NLoS channel as depicted in Fig. 1, where a line source spanning the linear region $\mathcal{L}_s \subset \mathbb{R}^2$ with length L_s transmits data to a line receiver spanning the linear region $\mathcal{L}_r \subset \mathbb{R}^2$ with length L_r . The two lines are parallel and oriented along the x -axis, with their centers aligned along the z -axis and separated by a distance d . Let $\mathbf{s} = [s_x, s_z]^T \in \mathcal{L}_s$ and $\mathbf{r} = [r_x, r_z]^T \in \mathcal{L}_r$ denote arbitrary points within the source and

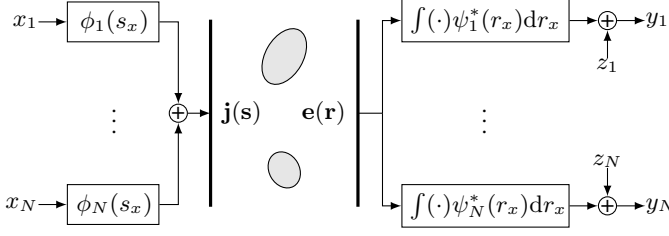


Fig. 1. A schematic of the considered WDM-based NLoS holographic MIMO system model.

receiver regions, respectively. Throughout the paper, we assume that the communication takes place via scalar waves (as in, e.g., [7], [8]), which simplifies the analysis by allowing the use of the scalar Green's function. The detailed electromagnetic (EM)-based channel model for holographic lines is presented in [9]. Let $\boldsymbol{\kappa} = [\kappa_x, \gamma(\kappa_x)]^T \in \mathbb{R}^2$ and $\mathbf{k} = [k_x, \gamma(k_x)]^T \in \mathbb{R}^2$ be the wave vectors corresponding to the transmit and receive propagation directions $\hat{\mathbf{k}} = \frac{\mathbf{k}}{\|\mathbf{k}\|}$ and $\hat{\boldsymbol{\kappa}} = \frac{\boldsymbol{\kappa}}{\|\boldsymbol{\kappa}\|}$, respectively. The corresponding wavenumbers are defined as $\kappa = k = \frac{2\pi}{\lambda}$, where λ is the wavelength. Following [9], the EM-based NLoS channel impulse response is given by

$$h(\mathbf{r}, \mathbf{s}) = \frac{1}{2\pi} \int_{\mathbb{R}^2} a_r(\mathbf{k}, \mathbf{r}) H_a(k_x, \kappa_x) a_s(\boldsymbol{\kappa}, \mathbf{s}) d\kappa_x d\kappa_x, \quad (1)$$

where $H_a(k_x, \kappa_x)$ represents the corresponding angular-domain channel impulse response (defined later) and

$$a_s(\boldsymbol{\kappa}, \mathbf{s}) = e^{-j\boldsymbol{\kappa}^T \mathbf{s}} = e^{-j(\kappa_x s_x + \gamma(\kappa_x) s_z)}, \quad (2a)$$

$$a_r(\mathbf{k}, \mathbf{r}) = e^{j\mathbf{k}^T \mathbf{r}} = e^{j(k_x r_x + \gamma(k_x) r_z)} \quad (2b)$$

are the transmit and receive plane waves, respectively.

In the presence of scatterers between the holographic lines, the one-to-one correspondence between the plane waves at the source and receiver no longer holds. Let $A(k_x, \kappa_x)$ be a non-negative function characterizing the scattering environment, referred to as the PSF, and let $W(k_x, \kappa_x)$ denote a spatially stationary complex white Gaussian noise random field. In particular, the PSF describes the coupling strength between the source and receiver. Under this model, the angular-domain channel is given by [7]

$$H_a(k_x, \kappa_x) = \frac{A(k_x, \kappa_x) W(k_x, \kappa_x)}{\sqrt{\gamma(k_x) \gamma(\kappa_x)}}, \quad (k_x, \kappa_x) \in \mathcal{D}^2, \quad (3)$$

with $\mathcal{D} = \{\kappa_x \in \mathbb{R} : -\kappa \leq \kappa_x \leq \kappa\}$ and

$$\gamma(\kappa_x) = \sqrt{\kappa^2 - \kappa_x^2}, \quad \kappa_x \in \mathcal{D} \quad (4)$$

for the traveling waves. Hence, plugging (3) into (1), the NLoS channel impulse response can be written as

$$h(\mathbf{r}, \mathbf{s}) = \frac{1}{2\pi} \int_{\mathcal{D}^2} a_r(\mathbf{k}, \mathbf{r}) \frac{A(k_x, \kappa_x) W(k_x, \kappa_x)}{\sqrt{\gamma(k_x) \gamma(\kappa_x)}} \times a_s(\boldsymbol{\kappa}, \mathbf{s}) d\kappa_x d\kappa_x, \quad (5)$$

where \mathcal{D}^2 specifies the support of the channel in the continuous wavenumber domain. Since $h(\mathbf{r}, \mathbf{s})$ is bandlimited within \mathcal{D}^2 , sampling this support as in [8] yields its discretized counterpart

formed by the sets

$$\mathcal{E}_s = \left\{ p_x \in \mathbb{Z} : -\kappa \leq \frac{2\pi}{L_s} p_x \leq \kappa \right\}, \quad (6a)$$

$$\mathcal{E}_r = \left\{ q_x \in \mathbb{Z} : -k \leq \frac{2\pi}{L_r} q_x \leq k \right\} \quad (6b)$$

at the source and receiver, respectively. Now, define $n_s = \text{card}(\mathcal{E}_s) = \lfloor \frac{2L_s}{\lambda} \rfloor$ and $n_r = \text{card}(\mathcal{E}_r) = \lfloor \frac{2L_r}{\lambda} \rfloor$ [10]. Following the Fourier plane-wave series expansion of a spatially stationary complex Gaussian random process from [8], we have

$$h(\mathbf{r}, \mathbf{s}) \approx \sum_{q_x \in \mathcal{E}_r} \sum_{p_x \in \mathcal{E}_s} H_a(q_x, p_x) a_r(q_x, \mathbf{r}) a_s(p_x, \mathbf{s}), \quad (7)$$

where

$$a_s(p_x, \mathbf{s}) = e^{-j(\frac{2\pi}{L_s} p_x s_x + \gamma(p_x) s_z)}, \quad (8a)$$

$$a_r(q_x, \mathbf{r}) = e^{j(\frac{2\pi}{L_r} q_x r_x + \gamma(q_x) r_z)} \quad (8b)$$

are the discretized counterparts of (2), with $\gamma(p_x) = \sqrt{\kappa^2 - (\frac{2\pi p_x}{L_s})^2}$ and $\gamma(q_x) = \sqrt{k^2 - (\frac{2\pi q_x}{L_r})^2}$, and

$$H_a(q_x, p_x) \sim \mathcal{N}_{\mathbb{C}}(0, \sigma^2(q_x, p_x)) \quad (9)$$

acts as a coupling coefficient characterizing the interaction between the transmit and receive plane waves.

III. WDM WITH EM-BASED NLoS CHANNEL

In this section, we first study the WDM-based NLoS channel in Section III-A, then derive its spatial autocorrelation properties in Section III-B, and finally characterize the resulting angular-domain channel in Section III-C. For simplicity, we set $s_z = 0$ and $r_z = d$; consequently, the source and receiver span the linear regions $\mathcal{L}_s = \{(s_x, 0) : |s_x| \leq \frac{L_s}{2}\}$ and $\mathcal{L}_r = \{(r_x, d) : |r_x| \leq \frac{L_r}{2}\}$, respectively.

A. WDM-Based NLoS Channel

Let $\{x_m\}_{m=1}^N$ denote the transmit data symbols, with $N \leq \min(n_s, n_r)$. The electric current at the source (measured in amperes) is constructed as $i(s_x) = \sum_{m=1}^N x_m \phi_m(s_x)$, where $\{\phi_m(s_x)\}_{m=1}^N$ represent the transmit Fourier basis, with m -th basis function

$$\phi_m(s_x) = \begin{cases} \frac{1}{\sqrt{L_s}} e^{j\frac{2\pi}{L_s} m s_x}, & |s_x| \leq \frac{L_s}{2} \\ 0, & \text{otherwise,} \end{cases} \quad (10)$$

and $x_m = \int_{-\frac{L_s}{2}}^{\frac{L_s}{2}} i(s_x) \phi_m^*(s_x) ds_x$. The current density at the source is defined as

$$\mathbf{j}(\mathbf{s}) = i(s_x) \delta(s_z) \hat{\mathbf{x}}, \quad (11)$$

where $\hat{\mathbf{x}} = [1, 0, 0]^T$ is the unit vector along the x -axis. The electric field at the receive point \mathbf{r} given the current density at the source in (11) is expressed as [8]

$$\begin{aligned} \mathbf{e}(\mathbf{r}) &= \int_{-\infty}^{\infty} h(\mathbf{r}, \mathbf{s}) \mathbf{j}(\mathbf{s}) ds \\ &= \int_{-\frac{L_s}{2}}^{\frac{L_s}{2}} h(\mathbf{r}, \mathbf{s}) \sum_{m=1}^N \xi_m \phi_m(s_x) \hat{\mathbf{x}} ds_x \\ &= [e_x(r_x), 0, 0]^T, \end{aligned} \quad (12)$$

with $h(\mathbf{r}, \mathbf{s})$ defined in (5). Then, $\mathbf{e}(\mathbf{r})$ is projected onto the inner-product space spanned by

$$\boldsymbol{\psi}_n(\mathbf{r}) = \psi_n(r_x)\delta(r_z - d)\hat{\mathbf{x}}, \quad (13)$$

where $\{\psi_n(r_x)\}_{n=1}^N$ represent the receive Fourier basis, with n -th basis function

$$\psi_n(r_x) = \begin{cases} \frac{1}{\sqrt{L_r}} e^{j\frac{2\pi}{L_r}nr_x}, & |r_x| \leq \frac{L_r}{2} \\ 0, & \text{otherwise.} \end{cases} \quad (14)$$

Hence, the n -th spatial sample of the received signal is given by

$$y_n = \int_{-\frac{L_r}{2}}^{\frac{L_r}{2}} \psi_n^*(r_x) e_x(r_x) dr_x + z_n, \quad (15)$$

where $z_n \in \mathcal{N}_{\mathbb{C}}(0, \chi^2)$ is the additive white Gaussian noise term with variance χ^2 . Finally, plugging (12) into (15) yields

$$y_n = \sum_{m=1}^N H_{n,m} x_m + z_n, \quad (16)$$

where

$$H_{n,m} = \int_{-\frac{L_r}{2}}^{\frac{L_r}{2}} \int_{-\frac{L_s}{2}}^{\frac{L_s}{2}} \psi_n^*(r_x) h(\mathbf{r}, \mathbf{s}) \phi_m(s_x) ds_x dr_x \quad (17)$$

is the WDM-based NLoS channel corresponding to the m -th transmit and n -th receive Fourier basis functions.

Combining (17) and (5) leads to

$$H_{n,m} = \frac{1}{2\pi} \int_{-\frac{L_r}{2}}^{\frac{L_r}{2}} \int_{-\frac{L_s}{2}}^{\frac{L_s}{2}} \int_{\mathbb{R}^2} \psi_n^*(r_x) a_r(\mathbf{k}, \mathbf{r}) \frac{A(k_x, \kappa_x)}{\sqrt{\gamma(k_x)}} \times \frac{W(k_x, \kappa_x)}{\sqrt{\gamma(\kappa_x)}} a_s(\boldsymbol{\kappa}, \mathbf{s}) \phi_m(s_x) dk_x d\kappa_x ds_x dr_x, \quad (18)$$

which is used in Section III-B to derive the spatial autocorrelation of $H_{n,m}$. Now, we substitute the Fourier series expansion of $h(\mathbf{r}, \mathbf{s})$, given in (7) with angular-domain channel impulse response in (9), into (17). Utilizing (8) along with the fact that $H_a(q_x, p_x)$ and $e^{j\frac{2\pi}{L_r}\gamma(q_x)r_x} H_a(q_x, p_x) e^{-j\frac{2\pi}{L_s}\gamma(p_x)s_x}$ are statistically equivalent, $H_{n,m}$ can be expressed with a slight abuse of notation as

$$\begin{aligned} H_{n,m} &= \frac{1}{\sqrt{L_r L_s}} \int_{-\frac{L_r}{2}}^{\frac{L_r}{2}} \int_{-\frac{L_s}{2}}^{\frac{L_s}{2}} \sum_{q_x \in \mathcal{E}_r} \sum_{p_x \in \mathcal{E}_s} H_a(q_x, p_x) \\ &\quad \times e^{j\frac{2\pi}{L_r}(q_x - n)r_x} e^{-j\frac{2\pi}{L_s}(p_x - m)s_x} ds_x dr_x \\ &= \sqrt{L_r L_s} \sum_{q_x \in \mathcal{E}_r} \sum_{p_x \in \mathcal{E}_s} H_a(q_x, p_x) \text{sinc}(q_x - n) \\ &\quad \times \text{sinc}(p_x - m) \\ &= \sqrt{L_r L_s} H_a(n, m), \end{aligned} \quad (19)$$

with $n \in \mathcal{E}_r$ and $m \in \mathcal{E}_s$. The characterization of $H_a(n, m)$ is presented in Section III-C. From (19), we observe that the channel resulting from applying WDM corresponds to the angular-domain channel scaled by a gain that depends on the lengths of the holographic lines.

B. Spatial Autocorrelation of $H_{n,m}$

In this section, we first derive the spatial autocorrelation of the WDM-based NLoS channel and then establish the relation

between its PSD and PSF. The spatial autocorrelation of the WDM-based NLoS channel is given by

$$R_{mn,qp} = \mathbb{E}[H_{n,m}(H_{p,q})^*]. \quad (20)$$

Since $W(k_x, \kappa_x)$ is a spatially stationary complex white Gaussian noise random field, we have $\mathbb{E}[W(k_x, \kappa_x)W^*(k'_x, \kappa'_x)] = \delta(k_x - k'_x)\delta(\kappa_x - \kappa'_x)$. Moreover, since $W(k_x, \kappa_x)$ and $e^{j\frac{2\pi}{L_r}\gamma(k_x)r_x} W(k_x, \kappa_x) e^{-j\frac{2\pi}{L_s}\gamma(\kappa_x)s_x}$ are statistically equivalent, plugging (18) into (20) leads to

$$\begin{aligned} R_{mn,qp} &= \frac{1}{(2\pi)^2} \int_{-\frac{L_r}{2}}^{\frac{L_r}{2}} \int_{-\frac{L_s}{2}}^{\frac{L_s}{2}} \int_{-\frac{L_r}{2}}^{\frac{L_r}{2}} \int_{-\frac{L_s}{2}}^{\frac{L_s}{2}} \int_{\mathbb{R}^2} \psi_n^*(r_x) \\ &\quad \times e^{jk_x(r_x - r'_x)} \psi_p(r'_x) \frac{A^2(k_x, \kappa_x)}{\gamma(k_x)\gamma(\kappa_x)} e^{-j\kappa_x(s_x - s'_x)} \\ &\quad \times \phi_m(s_x) \phi_q^*(s'_x) dk_x d\kappa_x ds_x dr_x ds'_x dr'_x. \end{aligned} \quad (21)$$

Considering separable scattering at the source and receiver [7], we have $A^2(k_x, \kappa_x) = A_r^2(k_x)A_s^2(\kappa_x)$ and (21) becomes

$$[\mathbf{R}]_{mn,qp} = [\mathbf{R}_s]_{m,q} [\mathbf{R}_r]_{n,p}, \quad (22)$$

where $\mathbf{R}_s \in \mathbb{C}^{n_s \times n_s}$ and $\mathbf{R}_r \in \mathbb{C}^{n_r \times n_r}$ denote the spatial autocorrelation matrices at the source and receiver, respectively, with

$$[\mathbf{R}_s]_{m,q} = \frac{1}{2\pi} \int_{-\frac{L_s}{2}}^{\frac{L_s}{2}} \int_{-\frac{L_s}{2}}^{\frac{L_s}{2}} \int_{-\infty}^{\infty} \phi_m(s_x) \frac{A_s^2(\kappa_x)}{\gamma(\kappa_x)} e^{-j\kappa_x(s_x - s'_x)} \times \phi_q^*(s'_x) d\kappa_x ds_x ds'_x, \quad (23a)$$

$$[\mathbf{R}_r]_{n,p} = \frac{1}{2\pi} \int_{-\frac{L_r}{2}}^{\frac{L_r}{2}} \int_{-\frac{L_r}{2}}^{\frac{L_r}{2}} \int_{-\infty}^{\infty} \psi_n^*(r_x) \frac{A_r^2(k_x)}{\gamma(k_x)} e^{jk_x(r_x - r'_x)} \times \psi_p(r'_x) dk_x dr_x dr'_x. \quad (23b)$$

Hence, (22) can be written in matrix form as

$$\mathbf{R} = \mathbf{R}_s \otimes \mathbf{R}_r \in \mathbb{C}^{n_r n_s \times n_r n_s}, \quad (24)$$

Comparing (23b) with the expression in [5, Eq. (71)], i.e.,

$$[\mathbf{R}_r]_{n,p} = \int_{-\frac{L_r}{2}}^{\frac{L_r}{2}} \int_{-\frac{L_r}{2}}^{\frac{L_r}{2}} \Gamma_r(r_x - r'_x) \psi_n^*(r_x) \psi_p(r'_x) dr_x dr'_x, \quad (25)$$

we have the ACF at the receiver given by

$$\begin{aligned} \Gamma_r(r_x) &= \frac{1}{2\pi} \int_{-\infty}^{\infty} \frac{A_r^2(k_x)}{\gamma(k_x)} e^{jk_x r_x} dk_x \\ &= \frac{1}{2\pi} \int_{-k}^k \frac{A_r^2(k_x)}{\sqrt{k^2 - k_x^2}} e^{jk_x r_x} dk_x, \end{aligned} \quad (26)$$

where the last equality follows from (4) for $k_x \in \mathcal{D}$. Applying the change of variable $k_x = k \cos \theta_r$, (26) simplifies to

$$\Gamma_r(r_x) = \frac{1}{2\pi} \int_0^\pi A_r^2(\theta_r) e^{jk \cos \theta_r r_x} d\theta_r. \quad (27)$$

The PSD at the receiver is obtained as the Fourier transform of the corresponding ACF in the wavenumber domain as

$$S_r(k_x) = \int_{-\infty}^{\infty} \Gamma_r(r_x) e^{-jk_x r_x} dr_x. \quad (28)$$

Plugging (26) into (28) and rearranging the order of integration yields

$$S_r(k_x) = \frac{1}{2\pi} \int_{-k}^k \frac{A_r^2(k'_x)}{\gamma(k'_x)} dk'_x \int_{-\infty}^{\infty} e^{j(k'_x - k_x)r_x} dr_x. \quad (29)$$

Now, using the relation $\int_{-\infty}^{\infty} e^{j(k'_x - k_x)r_x} dr_x = 2\pi\delta(k'_x - k_x)$, (29) simplifies to

$$S_r(k_x) = \frac{A_r^2(k_x)}{\gamma(k_x)} \mathbb{1}_{\mathcal{D}}(k_x), \quad (30)$$

which connects the PSD and PSF.

Under the assumption of separable scattering, we have $\sigma^2(n, m) = \sigma_s^2(m)\sigma_r^2(n)$, where $\sigma_s^2(m)$ and $\sigma_r^2(n)$ are the transmit and receive variances, respectively. Therefore, employing (19)–(20), we express the spatial autocorrelation as

$$R_{mn,qp} = L_s L_r \sigma_r^2(n) \sigma_s^2(m) \delta[n - p] \delta[m - q], \quad (31)$$

which can be written in matrix form as

$$\mathbf{R} = \text{diag}(\boldsymbol{\sigma}_s \odot \boldsymbol{\sigma}_s) \otimes \text{diag}(\boldsymbol{\sigma}_r \odot \boldsymbol{\sigma}_r), \quad (32)$$

where $\boldsymbol{\sigma}_s \in \mathbb{R}_+^{n_s}$ and $\boldsymbol{\sigma}_r \in \mathbb{R}_+^{n_r}$ collect the scaled standard deviations $\{\sqrt{L_s}\sigma_s(m) : m \in \mathcal{E}_s\}$ and $\{\sqrt{L_r}\sigma_r(n) : n \in \mathcal{E}_r\}$, respectively. Finally, comparing (24) with (32), we have

$$\mathbf{R}_s = \text{diag}(\boldsymbol{\sigma}_s \odot \boldsymbol{\sigma}_s), \quad (33a)$$

$$\mathbf{R}_r = \text{diag}(\boldsymbol{\sigma}_r \odot \boldsymbol{\sigma}_r). \quad (33b)$$

With (33), the WDM-based NLoS channel matrix can be obtained as

$$\mathbf{H} = \mathbf{R}_r^{\frac{1}{2}} \mathbf{W} \mathbf{R}_s^{\frac{1}{2}} \in \mathbb{C}^{n_r \times n_s}, \quad (34)$$

where $\mathbf{W} \in \mathbb{C}^{n_r \times n_s}$ is a random matrix with independent and identically distributed (i.i.d.) $\mathcal{N}_{\mathbb{C}}(0, 1)$ entries.

C. Characterization of the Angular-Domain NLoS Channel

Characterizing $H_a(n, m)$ is essential for deriving expressions for the WDM-based NLoS channel matrix. Since we have $H_a(n, m) \sim \mathcal{N}_{\mathbb{C}}(0, \sigma^2(n, m))$ from (9), the following analysis focuses on characterizing $\sigma^2(n, m)$. Equation (7) represents the Fourier series expansion of $h(\mathbf{r}, \mathbf{s})$ under the assumption that the normalized lengths at the source and receiver are large, i.e., $\frac{L_s}{\lambda} \gg 1$ and $\frac{L_r}{\lambda} \gg 1$. In this setting, $\sigma^2(n, m)$ is obtained as the sampled value of the PSD at the point $(\frac{2\pi}{L_r}n, \frac{2\pi}{L_s}m)$ in the wavenumber domain [11, Eq. (177)]. Since separable scattering implies $\sigma^2(n, m) = \sigma_s^2(m)\sigma_r^2(n)$ (see Section III-B), we focus on modeling the variance at the receiver, as the procedure for the source follows analogously.

The variance at the receiver after performing a change of variable similar to (27) and utilizing (30) is given by

$$\sigma_r^2(n) = \frac{1}{2\pi} \int_{\mathcal{T}_r(n)} A_r^2(\theta_r) d\theta_r, \quad (35)$$

with $\mathcal{T}_r(n) = \{\arccos(\frac{\lambda}{L_r}(n+1)), \arccos(\frac{\lambda}{L_r}n)\}$; the detailed steps are presented in [9]. The PSF is determined by $\tilde{A}_r^2(\theta_r) = \frac{A_r^2(\theta_r)}{2\pi}$, which is modeled as a mixture of two-dimensional (2D) von Mises-Fisher (vMF) distributions [7], i.e.,

$$\tilde{A}_r^2(\theta_r) = \sum_{\ell=1}^C w_{\ell} p_{\ell}(\theta_r), \quad (36)$$

where C denotes the number of scattering clusters, $p_{\ell}(\theta_r)$ is the 2D vMF distribution for the ℓ -th cluster, and the positive weights are such that $\sum_{\ell} w_{\ell} = 1$. Let $I_0(\cdot)$ and $I_1(\cdot)$ denote the modified Bessel functions of the first kind and order zero and one, respectively. The 2D vMF distribution is defined as [12]

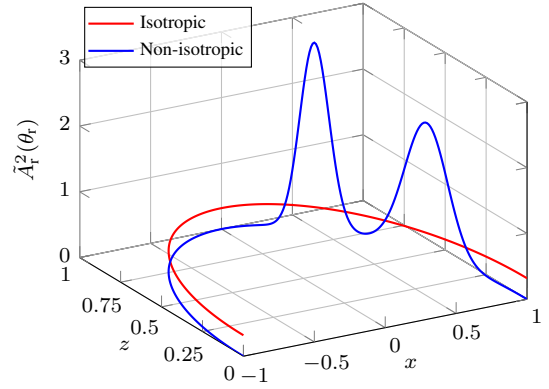


Fig. 2. Illustration of $\tilde{A}_r^2(\theta_r)$.

$$p_{\ell}(\theta_r) = \frac{1}{2\pi I_0(\alpha_{\ell})} \exp(\alpha_{\ell} \cos(\theta_r - \bar{\theta}_{r,\ell})), \quad \theta_r \in [-\pi, \pi], \quad (37)$$

where $\alpha_{\ell} \in \mathbb{R}^+$ is the concentration parameter and $\bar{\theta}_{r,\ell} \in [-\pi, \pi]$ is the mean angle of the ℓ -th cluster. For a given normalized circular variance $\nu_{\ell}^2 \in [0, 1]$, we compute α_{ℓ} using the fixed-point equation $\nu_{\ell}^2 = 1 - \left(\frac{I_1(\alpha_{\ell})}{I_0(\alpha_{\ell})}\right)^2$.

We now consider the case of isotropic scattering, obtained by setting $C = 1$ with $\alpha_1 = 0$, which implies $\nu_1^2 = 1$. Considering only the forward-traveling wave, i.e., $\theta_r \in [0, \pi)$, and using (36)–(37), we have

$$\tilde{A}_r^2(\theta_r) = \frac{1}{\pi}, \quad \theta_r \in [0, \pi). \quad (38)$$

In this case, since (38) no longer depends on $\bar{\theta}_r$, (27) can be expressed as $\Gamma_r(r_x) = J_0(kr_x)$, where $J_0(\cdot)$ is the Bessel function of the first kind and order zero, and the corresponding PSD is given by $S_r(k_x) = \frac{2}{\sqrt{k^2 - k_x^2}}, |k_x| \leq k$. Hence, under isotropic scattering, the PSD and ACF coincide with the classical Jakes' isotropic model.

IV. NUMERICAL RESULTS

We consider holographic lines with lengths $L_s = L_r = 128\lambda$ and wavelength $\lambda = 0.01$ m (corresponding to a carrier frequency of 30 GHz). We compare the WDM-based NLoS channel with i.i.d. Rayleigh fading and Jakes' isotropic models, which are obtained by spatially sampling the holographic lines according to the Nyquist criterion, i.e., with $\frac{\lambda}{2}$ spacing. To simplify the analysis, we assume symmetric scattering between the source and receiver, i.e., $\tilde{A}_s^2(\theta_s) = \tilde{A}_r^2(\theta_r)$, which yields $\sigma_r^2(n) = \sigma_s^2(m)$. For non-isotropic scattering, we consider $C = 2$ scattering clusters with mean angles $\bar{\theta}_{r,1} = 30^\circ$ and $\bar{\theta}_{r,2} = 60^\circ$, with normalized circular variances $\nu_1^2 = 0.01$ and $\nu_2^2 = 0.005$, respectively, and weights $w_1 = w_2 = \frac{1}{2}$. Fig. 2 illustrates $\tilde{A}_r^2(\theta_r)$ for isotropic and non-isotropic scattering obtained using (38) and (36)–(37), respectively, for the forward-traveling waves, i.e., $\theta_r \in [0, \pi)$.

We examine the DoF defined as follows: for isotropic scattering, they are the minimum number of non-zero coupling coefficients in \mathcal{E}_s and \mathcal{E}_r required to represent $h(\mathbf{r}, \mathbf{s})$ over the linear regions \mathcal{L}_s and \mathcal{L}_r [10], i.e., $\text{DoF}_{\text{iso}} = \min(n_s, n_r)$; for non-isotropic scattering, they coincide with the DoF of the underlying random process [13], i.e.,

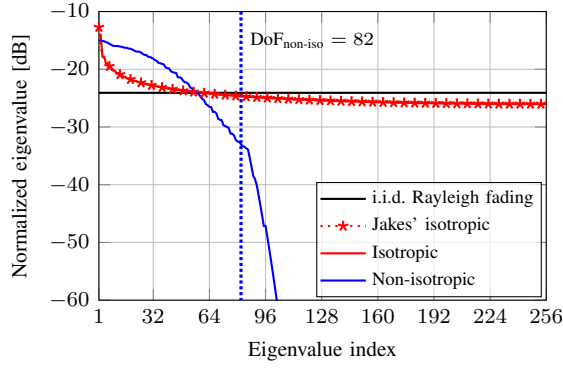


Fig. 3. Normalized eigenvalues of \mathbf{R}_r .

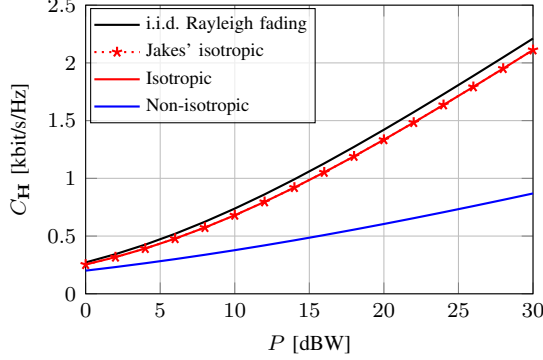


Fig. 4. Ergodic capacity versus total transmit power.

$$\text{DoF}_{\text{non-iso}} = \min \left\{ n'_s : \sum_{i=1}^{n'_s} \sigma_{s,i}^2 \geq 1 - \epsilon, n'_r : \sum_{i=1}^{n'_r} \sigma_{r,i}^2 \geq 1 - \epsilon \right\}, \quad (39)$$

where ϵ specifies the desired level of accuracy and $\{\sigma_{s,i}^2\}_{i=1}^{n'_s}$ and $\{\sigma_{r,i}^2\}_{i=1}^{n'_r}$ represent $\{\sigma_s^2(m) : m \in \mathcal{E}_s\}$ and $\{\sigma_r^2(n) : n \in \mathcal{E}_r\}$, respectively, obtained as in (35) and sorted in decreasing order. As done in [14], we set $\epsilon = 0.3\%$ according to the three-sigma rule of the Gaussian distribution, stating that about 99.7% of the values lie within three standard deviations. Fig. 3 plots the eigenvalues of the receive spatial autocorrelation matrix \mathbf{R}_r (normalized by its trace). For i.i.d. Rayleigh fading, the channel entries are mutually independent, leading to identical eigenvalues of \mathbf{R}_r . The closest physically meaningful counterpart is Jakes' isotropic model, whose spatial autocorrelation matrix is obtained from the spatial sampling of $J_0(kr_x)$. The normalized eigenvalues under isotropic scattering coincide with those of Jakes' isotropic model, whereas the non-isotropic case exhibits a significantly steeper decay, indicating stronger spatial correlation. In terms of DoF, we have $\text{DoF}_{\text{iso}} = 256$ and $\text{DoF}_{\text{non-iso}} = 82$.

Considering (16) and assuming perfect channel state information at both the source and receiver, the ergodic capacity (measured in bits/s/Hz) is given by

$$C_{\mathbf{H}} = \mathbb{E} \left[\sum_{i=1}^N \log_2 \left(1 + \frac{P_i}{\chi^2} \varrho_i(\mathbf{H}\mathbf{H}^H) \right) \right], \quad (40)$$

where $\varrho_i(\cdot)$ denotes the i -th eigenvalue of $\mathbf{H}\mathbf{H}^H$ sorted in decreasing order, P_i is the transmit power allocated to the i -th eigenmode, computed via water-filling for each channel

realization, and $P = \sum_{i=1}^N P_i$ represents the total transmit power. For simplicity, we assume $\chi^2 = 0$ dBW and compute (40) by averaging over 500 independent channel realizations. Fig. 4 depicts the ergodic capacity against the total transmit power. With water-filling power allocation, the capacity reflects the eigenvalue distribution of \mathbf{R}_r . The curve corresponding to Jakes' isotropic model closely matches that of isotropic scattering. The non-isotropic case yields the lowest capacity due to the stronger spatial correlation and the correspondingly smaller number of dominant eigenmodes. The capacity under i.i.d. Rayleigh fading also approaches that of the isotropic and Jakes' models.

V. CONCLUSIONS

We analyzed the WDM-based NLoS channel in holographic MIMO by characterizing its spatial autocorrelation. In particular, we showed that applying WDM to the NLoS channel leads to its angular-domain representation. Furthermore, particularizing the analysis to isotropic scattering recovers Jakes' isotropic model. The results highlight that WDM serves not only as a multiplexing technique but also as an effective analytical tool for studying holographic MIMO channels. Future work may explore extensions to the multi-user setting.

REFERENCES

- [1] I. Atzeni *et al.*, "Sub-THz communications: Perspective and results from the Hexa-X-II project," *IEEE Open J. Commun. Soc.*, vol. 6, pp. 7495–7540, 2025.
- [2] L. Wei *et al.*, "Electromagnetic information theory for holographic MIMO communications," 2024. [Online]. Available: <https://arxiv.org/pdf/2405.10496>
- [3] A. Sharma, A. Prajapati, and P. Pinho, "Interference-aware antenna synthesis for enhanced coverage in intelligent transportation system," *IEEE Trans. Veh. Technol.*, vol. 70, no. 8, pp. 7803–7811, 2021.
- [4] C. Huang *et al.*, "Holographic MIMO surfaces for 6G wireless networks: Opportunities, challenges, and trends," *IEEE Wireless Commun.*, vol. 27, no. 5, pp. 118–125, 2020.
- [5] L. Sanguinetti, A. A. D'Amico, and M. Debbah, "Wavenumber-division multiplexing in line-of-sight holographic MIMO communications," *IEEE Trans. Wireless Commun.*, vol. 22, no. 4, pp. 2186–2201, 2022.
- [6] A. A. D'Amico, L. Sanguinetti, and M. Debbah, "Performance analysis of WDM in LoS communications with arbitrary orientation and position," *IEEE Wireless Commun. Lett.*, vol. 11, no. 9, pp. 1880–1884, 2022.
- [7] A. Pizzo, L. Sanguinetti, and T. L. Marzetta, "Spatial characterization of electromagnetic random channels," *IEEE Open J. Commun. Soc.*, vol. 3, pp. 847–866, 2022.
- [8] A. Pizzo, T. Marzetta, and L. Sanguinetti, "Holographic MIMO communications under spatially-stationary scattering," *Proc. Asilomar Conf. Signals, Syst., and Comput. (ASILOMAR)*, 2020.
- [9] A. Prajapati, P. Dharmawansa, M. Di Renzo, and I. Atzeni, "LoS+NLoS holographic MIMO: Analysis and application of wavenumber-division multiplexing," *IEEE Trans. Wireless Commun. (submitted)*, 2025.
- [10] A. Pizzo, T. L. Marzetta, and L. Sanguinetti, "Degrees of freedom of holographic MIMO channels," in *Proc. IEEE Int. Workshop Signal Process. Adv. in Wireless Commun. (SPAWC)*, 2020.
- [11] H. L. Van Trees, *Detection, Estimation, and Modulation Theory, Part I: Detection, Estimation, and Linear Modulation Theory*. John Wiley & Sons, 2004.
- [12] K. Mardia and P. Jupp, *Directional Statistics*. John Wiley & Sons, 2000.
- [13] M. Franceschetti, *Wave Theory of Information*. Cambridge University Press, 2017.
- [14] A. Pizzo, L. Sanguinetti, and T. L. Marzetta, "Fourier plane-wave series expansion for holographic MIMO communications," *IEEE Trans. Wireless Commun.*, vol. 21, no. 9, pp. 6890–6905, 2022.